Perphenazine-macrocycle conjugates divert Aβ42 towards non-toxic aggregates by monomer sequestration.

Sarah R Ball[1], Julius S P Adamson[2], Michael A Sullivan[1], Manuela R Zimmermann[3], Victor Lo[1], Maximo Sanz-Hernandez[1], Frank Jiang[2], Ann H. Kwan[4], Eryn L Werry[2, 5], Tuomas P J Knowles[3, 6], Michael Kassiou[2], Georg Meisl[3], Matthew H Todd[7], Peter J Rutledge[2*] and Margaret Sunde[1*].

[1]Discipline of Pharmacology, The University of Sydney, Sydney, Australia. [2]School of Chemistry, The University of Sydney, Sydney, Australia. [3]Centre for Misfolding Diseases, Department of Chemistry, University of Cambridge, Cambridge UK. [4]School of Life and Environmental Sciences, The University of Sydney, Sydney, Australia. [5]Brain and Mind Centre, The University of Sydney. [6]Cavendish Laboratory, University of Cambridge, JJ Thomson Avenue, CB4 0HE, UK. [7]School of Pharmacy, University College London, London UK.

*Co-corresponding authors: Margaret Sunde and Peter Rutledge

Email: margaret.sunde@sydney.edu.au; peter.rutledge@sydney.edu.au

Classification

Biological Sciences; Biophysics and Computational Biology

Keywords

amyloid, inhibition, kinetic analysis, monomer sequestration, Alzheimer's disease

Abstract

The amyloid-β peptide, the main protein component of amyloid plaques in Alzheimer's disease, plays a key role in the neurotoxicity associated with the condition through the formation of small toxic oligomer species which mediate the disruption of calcium and glutamate homeostasis. The lack of therapeutic benefit associated with removal of mature amyloid-β fibrils has focused attention on the toxic oligomeric species formed during the process of fibril assembly. Here, we present the design and synthesis of a family of perphenazine-macrocyle conjugates. We find that two-armed perphenazine-cyclam conjugates divert the monomeric form of the amyloid-β peptide away from the amyloidogenic pathway into amorphous aggregates that are not toxic to differentiated SH-SY5Y cells *in vitro.* This strategy prevents the formation of damaging amyloid oligomers. Kinetic analysis of the effects of these compounds on the assembly pathway, together with NMR spectroscopy, identifies rapid monomer sequestration as the underlying neuroprotective mechanism. The ability to specifically target the monomeric form of amyloid-β allows for further understanding of the impact of the multiple species formed between peptide biogenesis and plaque deposition. The modular, three-dimensional structure of these compounds provides a starting point for the design of more potent modulators of this amyloid-forming peptide, and can be adapted to probe the protein self-assembly pathways associated with other proteinopathies.

Significance statement

The aggregation pathway of the amyloid-β (Aβ) peptide in Alzheimer's disease is complex and involves multiple different species. An inability to isolate and study the impact of distinct Aβ species has undermined efforts to develop effective therapies. To address this issue, we have developed a series of molecules that specifically sequester the monomeric form of the highly aggregation-prone Aβ42 peptide. Interaction with these molecules diverts Aβ42 from the amyloidogenic pathway and prevents formation of toxic oligomeric species. We use kinetic analysis and NMR spectroscopy to identify rapid monomer sequestration as the underlying neuroprotective mechanism. Future rational development of these molecules and characterisation of their interactions with Aβ will delineate the impact of different Aβ oligomers on neurobiology and pathology.

Introduction

Alzheimer's disease (AD) is the most common form of dementia and one of the most devastating diseases of the current age. Despite AD affecting around 50 million people worldwide, and imposing huge physical, social and economic impacts, there are currently still no approved disease-modifying therapies. AD is a neurodegenerative disease associated with protein misfolding and misprocessing, resulting in aggregation and accumulation: a proteinopathy. It is characterised by the extracellular deposition of amyloid-β (Aβ) plaques and the presence of intracellular neurofibrillary tangles (NFTs) composed of the tau protein. Both the Aβ plaques and the NFTs have an amyloid structure (1-3).

The Aβ peptide is a cleavage product of the membrane-bound amyloid precursor protein (APP). Two major isoforms of Aβ are detected in cerebrospinal fluid and plasma: Aβ40 and Aβ42. Genetic and biomarker studies suggest that an imbalance in the production and processing of Aβ peptides plays a role in the AD process (4). Although the full sequence of critical molecular events that lead to neuronal death is yet to be defined, self-assembly of the Aβ peptide into soluble oligomers and amyloid fibrils has been shown to generate neurotoxic oligomeric species (5-7). These oligomers impact neuronal activity through effects on cell membranes, calcium homeostasis, and glutamate reuptake, amongst other deleterious mechanisms (8-14).

In order to form Aβ amyloid fibrils, Aβ monomers must initially form a nucleus, through a process referred to as primary nucleation (Fig. 1A). Recruitment of additional monomers leads to the formation of soluble oligomers with a range of sizes. Oligomers undergo a conformational change to generate higher molecular weight fibrillar structures that mature into fibrils consisting of two protofilaments with a cross-β structure (15). Such mature fibrils offer sites for elongation at their ends, and secondary nucleation on their lateral surfaces (1, 16) (Fig. 1A). Thus, Aβ amyloid formation is a complex, multiple-step process with many species existing in parallel (17).

The failure of clinical trials aimed at reducing the accumulation of mature Aβ fibrils in extracellular plaques has seen efforts shift towards intervention at earlier stages in the pathway, with the aim of inhibiting formation of toxic, pre-fibrillar oligomers (18). Several small-molecule compounds have been shown to target different stages of Aβ oligomerisation and amyloid formation *in vitro*, via mechanisms including suppression of primary nucleation or acceleration of fibril formation (19-21). Polyphenols such as epigallocatechin gallate (EGCG) and brazilin have also been explored for their ability to shift the amyloid formation pathway to amorphous aggregates (22-25). Some of these compounds have shown promise in animal models but are yet to show efficacy in clinical trials (26).

We have developed a series of molecules designed to divert Aβ away from the pathway that generates neurotoxic oligomers and amyloid fibrils. These are derivatives of the azamacrocycle cyclam, connected to perphenazine through a triazole linker, that are able to coordinate to a central metal ion via the macrocycle *and* the pendant triazole (Fig. 1B). We have shown previously that cyclam derivatives with triazole-linked pendant groups can adopt a range of different, defined pendant geometries depending on the connectivity of the triazole linker and the metal ion coordinated by the macrocycle (27, 28), and that cyclam complexes with peptide pendants can rescue neuronal cells from Aβ-induced cytotoxicity (29). Combining these insights with the documented capacity of polymeric perphenazine conjugates to modulate amyloid aggregation (30), we designed a series of compounds in which cyclam is linked via click-derived triazoles to pendant groups that are known to interact with Aβ (perphenazine, dopamine), along with simpler naphthyl derivatives as control compounds (SI, Fig. S1A).

We show here that three of these novel molecules can divert the Aβ formation pathway towards the generation of amorphous aggregates that are not toxic to differentiated, neuron-like SH-SY5Y cells. Quantitative analysis of the effects these molecules have on Aβ42 amyloid assembly (by comparison of experimental kinetic data with kinetic curves generated by analytical solution of the rate laws of aggregation) reveals that they act through a distinct monomer sequestration process. Interaction of Aβ42 monomer with the inhibitors results in the formation of non-fibrillar aggregates. By preventing

the on-pathway conversion of Aβ42 monomer to mature amyloid fibrils, these compounds reduce the population of toxic oligomer species. This study provides the first demonstration of a reduction in neurotoxicity as a result of Aβ42 monomer sequestration. These molecules serve as tools which allow the dissection of the Aβ assembly pathway and will improve our understanding of the impact of different Aβ oligomers on neurobiology and pathology.

Results

Perphenazine-cyclam conjugates inhibit Aβ42 amyloid assembly

A series of cyclam conjugates was designed to enable a systematic investigation of the Aβ aggregation and amyloid assembly pathways. Six parent cyclam derivatives were prepared: the mono-substituted naphthyl (**C1**), dopamine (**C4**) and perphenazine (**C7**) analogues, and corresponding bis-substituted compounds with naphthyl (**C10**), dopa (**C13**) and perphenazine (**C16**) pendants, along with their zinc(II) and copper(II) complexes (mono-naphthyl **C2**, **C3**; mono-dopa **C5**, **C6**; mono-perphenazine **C8**, **C9**; bis-naphthyl **C11**, **C12**; bis-dopa **C14**, **C15**; and bis-perphenazine **C17**, **C18**) (SI Fig. S1A). Initial screening of these compounds showed the bis-perphenazine analogues (ligand **C16** and its copper(II) (**C18**) complex) to have promising capacity to suppress amyloid formation by synthetic Aβ42 (SI, Fig. S1B).

All three bis-perphenazine derivatives **C16**, **C17** and **C18** showed a similar ability to inhibit amyloid formation by Aβ40 and Aβ42 (SI, Fig. S1C,D). We have focused this work on Aβ42 because the sequence difference of two amino acids confers an increased aggregation propensity on Aβ42 compared to Aβ40 (31) and a reduction in plasma Aβ42 levels is associated with an increase in amyloid deposition (32). Recombinant Aβ42 was prepared using the methods described by Linse and colleagues (33, 34). This resulted in a monomeric form of Aβ42 that generated highly reproducible kinetics for amyloid assembly (SI, Fig. S2). The three cyclam/ bis-perphenazine conjugates **C16**, **C17** and **C18** were found to be potent inhibitors of Aβ42 amyloid formation, as monitored by ThT fluorescence (Fig. 2; SI Fig. S3 and Fig. S4).

The inhibitors demonstrated a concentration-dependent effect, and at a 1:5 molar ratio of Aβ42:compound, using 10 µM Aβ42, amyloid assembly was almost completely suppressed, as judged by the reduction in the level of Thioflavin T (ThT) fluorescence observed (Fig. 2A). Assays at lower Aβ42 concentration, using a range of inhibitor concentrations that allowed the plateau phase of amyloid assembly to be reached, revealed that all three compounds also introduce an increase in lag phase. The length of the lag phase increases with increasing inhibitor concentration (Fig. 2B). The zinc(II) complex **C17** displayed the strongest inhibition, followed by copper(II) complex **C18**, and the uncomplexed ligand **C16**, highlighting the influence of the central metal ion on the three-dimensional shape of the inhibitor – in particular the relative orientation of the two perphenazine pendants – and resulting impact on the mechanism of Aβ42 amyloid inhibition.

Perphenazine alone does not display strong inhibition of Aβ42 amyloid formation in this ThT assay, highlighting the fact that it is not the perphenazine moiety *per se* that is responsible for the inhibitory activity (SI Fig. S5). The observed inhibition is also not due to an effect of unchelated metal ions directly on Aβ42. Previous studies have demonstrated that Zn(II) and Cu(II) cations can themselves inhibit Aβ42 amyloid formation (35-37), reflected by an increase in the lag phase or a decrease in the observed ThT intensity (SI Fig. 6A). However, we observed that **C17** and **C18** remain effective inhibitors of Aβ amyloid formation even in the presence of the chelating agent EDTA, which would sequester any free metal ions and block their inhibitory capacity (SI Fig. 6B).

The perphenazine conjugates divert Aβ42 from amyloid assembly towards amorphous aggregates

A sensitive protein concentration assay confirmed that when the plateau of assembly was reached, in samples containing Aβ42 only, or Aβ42 in the presence of a 5-fold molar excess of inhibitor, all Aβ42 was converted to an insoluble form that was readily pelleted by centrifugation (SI Fig. S7).

Transmission electron microscopy was used to examine the final morphology of the Aβ42 material present after ~40 h incubation with compounds or 1% DMSO as control. An inhibitor concentration dependent shift from the characteristic fibrillar morphology of Aβ42 amyloid (Fig. 3A) to amorphous aggregates (Fig. 3B, C & D) was observed. The amorphous aggregates had a beads-on-a-string appearance, with the "beads" approximately 20 nm wide and the "strings" >1 µm in length. Only amorphous material was observed when Aβ42 was incubated in the presence of **C16**, even at 1:1 molar ratio of **C16**:Aβ42, while a combination of fibrillar and amorphous material was observed in samples prepared at 1:1 molar ratios of **C17**:Aβ42 and **C18**:Aβ42 (SI Fig. S8).

The perphenazine conjugates reduce neurotoxicity associated with Aβ oligomers

Although uncertainty about the precise nature of the deleterious oligomeric species formed by Aβ42 remains, many groups have demonstrated that soluble intermediate species formed by Aβ42 *in vitro* are cytotoxic (5). Accordingly, the ability of compounds **C16**–**C18** to prevent the formation of toxic Aβ42 species was indexed using SH-SY5Y cells which had been differentiated to an AD-appropriate phenotype by treatment with retinoic acid and brain-derived neurotrophic factor (38). Freeze-dried monomeric Aβ42 was treated with hexafluoro-2-propanol (HFIP), lyophilised and then resuspended in PBS, before being diluted in cell media and added immediately to cells. Aβ42 fibrils were prepared by incubating monomeric Aβ42 solution in cell media at 37 °C for 24 hours, a time point significantly past the plateau level in unshaken ThT experiments using cell media (SI Fig. S9). The compounds were added to differentiated SH-SY5Y cells alone, or added together with Aβ42 in a monomeric or fibrillar form. After 24 hours, the number of metabolically-active cells was measured using a CTB fluorescence assay. The CellTiter-Blue® (CTB) assay of cell viability was chosen, given published concerns regarding the use of MTT with Aβ42 (5).

By themselves, compounds **C16**, **C17** and **C18** displayed no significant toxicity towards differentiated SH-SY5Y cells, relative to vehicle only (Fig. 4A). Exposure of these cells to freshly prepared monomeric Aβ42 resulted in significant ($P < 0.001$) toxicity compared to vehicle, as expected due to the generation of oligomeric species, and the addition of **C16**, **C17** or **C18** led to significant protection against this neurotoxicity (Fig. 4B). Perphenazine was not cytotoxic by itself and imparted a similar level of protection as **C16**, **C17** and **C18**. These results contrast with the observed neurotoxicity of EGCG at the same concentrations and the lack of protection by this polyphenol against cytotoxicity induced by addition of monomeric Aβ42 (Fig. 4A,B). When Aβ42 was prepared in fibrillar form and then added to cells, no cytotoxicity was observed with fibrils alone or in the presence of compounds (Fig. 4C). Following from these experiments, independent concentration response assays were performed with **C16**. The IC_{50} for **C16** was determined to be 2.33 µM ($n = 3$; SD = 0.89) (Fig. 4D). Here we have used an established assay of neurotoxicity, with differentiated SH-SY5Y cells and well-characterised preparations of monomeric and fibrillar Aβ42. Although the origins of the neurotoxicity resulting from the conversion of Aβ42 from monomeric to fibrillar form *in vitro* are not defined, these results provide clear evidence that the generation of amorphous Aβ42 aggregates in the presence of **C16**–**C18** prevents the formation of neurotoxic species.

C16, C17 and C18 inhibit Aβ amyloid formation through sequestration of Aβ42 monomers

The microscopic processes underlying amyloid formation of Aβ42 are primary nucleation, elongation and secondary nucleation (39, 40). Their relative importance can be quantified through their rate constants, obtained by fitting integrated rate laws within the framework of chemical kinetics (41). Data measured at 2.5 µM and 10 µM Aβ42, in the presence of a range of concentrations of inhibitor, were analysed using the online fitting software AmyloFit. The rate constants of the unperturbed systems agreed well with similar experiments (16). To probe the mechanism of action of the inhibitory compounds **C16**, **C17** and **C18**, we varied systematically one rate constant in the rate law, or the level of available monomer, respectively (41). By comparing how well these modified rate laws can describe the data, a mechanism that primarily involves inhibition of primary nucleation could be ruled

out for **C16**, **C17** and **C18** (Fig. 5A, B and SI Fig. S10-14) as the origin of the changes in the kinetic behaviour in the presence of the inhibitor.

The introduction of small numbers of preformed fibril seeds at the beginning of the aggregation reaction can be used to bypass primary nucleation. As predicted by the finding that primary nucleation was not affected by the presence of inhibitors, these compounds remain effective as inhibitors of Aβ42 amyloid fibril formation even when exogenous fibril seeds are present (Fig. 2C). In the presence of 2% or 5% seeds, and the presence of **C16–C18** at 1:2.5 or 1:5 Aβ42:compound molar ratio resulted in inhibition of Aβ42 assembly, similar to the level of inhibition observed in the absence of pre-formed seeds (SI Fig. S15). In addition to ruling out the blocking of primary nucleation as the source of the inhibitory effect, the results observed in the presence of seeds, when the aggregation reaction reaches completion much sooner, suggest that binding of the compounds to the monomeric form of Aβ42 occurs rapidly.

Based on the fits to the normalised kinetic data alone, mechanisms based on inhibition of secondary nucleation, inhibition of elongation, and monomer sequestration were similarly likely as the main modes of action of the compounds (SI Fig. S10-14). However, we found a clear correlation between the ThT intensity at completion of the aggregation reaction and the effective monomer concentration determined from the fits (Fig. 5D, E, F insets). As the fitting was performed on normalised kinetic data, these two quantities constitute independent measures of the same physical property. The correlation between an equilibrium measure, the plateau level, and a parameter estimated on the basis of normalised kinetics, the effective monomer concentration, provides further independent evidence for monomer sequestration by the inhibitors. In addition to accounting for the delay in aggregation and decrease in ThT signal, monomer sequestration by the inhibitors also provides a mechanistic explanation for the appearance of amorphous material as discussed above. The fits assumed that this monomer sequestration proceeds much faster than aggregation and can thus be modelled by a reduced effective monomer concentration. The observed results in the presence of seeds, when the aggregation reaction reaches completion much sooner, suggest that binding of the compounds to the monomeric form of Aβ42 indeed occurs rapidly.

Further support for monomer sequestration as the dominant mode of inhibition of Aβ42 aggregation by **C16**, **C17** and **C18** was gained by obtaining consistent values for the apparent dissociation constant of monomer and inhibitor, K_D, by orthogonal methods. First, the effective monomer concentration obtained through the chemical kinetics analysis at different monomer and inhibitor concentrations was used to construct monomer-inhibitor binding curves (Fig. 5D, E, F). To fit these data, we assumed a simple one-to-one binding, yielding K_D values of 7.6 μM (95% CI, 6.6–9.1) for **C16**, 5.7 μM (95% CI, 4.6–7.1) for **C17** and 7.4 μM (95% CI, 6.2–9.1) for **C18**.

Secondly, we utilised one-dimensional ^{1}H NMR spectroscopy to determine an apparent binding constant for the interaction between the inhibitors and Aβ42. For each of **C16**, **C17** and **C18**, inhibitor was titrated into a solution containing 10 μM unlabelled Aβ42, over the inhibitor concentration range of 1 – 50 μM. A decay profile in the protein signal intensity across the spectrum was observed with increasing concentration of all three inhibitors (Fig. 6 and SI Fig. S16). A 5:1 ratio of inhibitor:Aβ42 resulted in a reduction of proton signals to baseline, consistent with the sequestration of monomer into very large and/or insoluble assemblies, the precipitation of material during the course of the NMR titrations, and the amorphous aggregates observed by TEM (Fig. 3). The signal decay curves were fitted to a quadratic equation for the calculation of the apparent K_D of each compound, yielding 4.6 μM (95% CI, 3.1–6.5) for **C16**, 3.4 μM (95% CI, 2.2–4.9) for **C17** and 3.7 μM (95% CI, 2.4–5.3) for **C18**. The observed effect of these perphenazine cyclam conjugates on Aβ42 assembly is different to that of the polyphenol EGCG, where the presence of EGCG results in only a small decrease in the observed ^{1}H spectrum signal from Aβ42, up to 31% signal loss at a 5-fold excess of small molecule (Fig. 6D and SI Fig. S16). This is evidence that upon addition of EGCG, the monomeric Aβ42 species is still the most prevalent in the sample. In contrast, when the less aggregation-prone Aβ40 interacts with

EGCG, specific interactions are observed by solution NMR and it forms insoluble oligomers that are in equilibrium with soluble Aβ40 (42).

A monomeric sample of recombinant ^{15}N-labeled Aβ42 was prepared and analysed in the absence and presence of **C16** to probe the regions of the polypeptide involved in the interaction. The ^{15}N HSQC spectrum collected in the absence of any added compound reflected the high quality of the recombinant, monomeric Aβ42 sample and the chemical shifts were superimposable upon those reported by others previously for Aβ42 (43). Addition of **C16** resulted in an immediate reduction in signal intensity that was uniform across all peaks in the spectrum (SI Fig. S17). Protein that is not sequestered into an amorphous aggregate remains in the solution at the 1:1 ratio of protein:inhibitor. No peak-specific changes in signal intensity or chemical shift were detected that could be attributed to binding of **C16** to a distinct region of monomeric Aβ42. Instead, the loss of signal is consistent with the binding of monomer to **C16** resulting in the generation of a conformation that is highly aggregation-prone and rapidly forms large structures, undetectable by solution NMR.

Discussion

We have designed a class of compounds that specifically sequester the monomeric form of Aβ42 into non-fibrillar assemblies that are different to the cytotoxic oligomeric forms associated with Aβ42 amyloid formation. The process by which monomeric Aβ42 converts to the mature fibrillar form detected in amyloid plaques is complex and non-linear. It involves multiple oligomeric and prefibrillar species that may act as reactants, products, intermediates, and catalysts of the process and contribute to toxicity to different extents. The challenge posed to health and social systems by AD has stimulated a multitude of different approaches to inhibition of Aβ42 amyloid formation. The ability to interrogate a change in aggregation kinetics caused by an inhibitor and thereby identify the mechanism of inhibition offers new opportunities to understand the consequences of intervention at defined points within the Aβ42 assembly pathway. Many studies of peptide-based inhibitors that incorporate “disruption elements” report success in preventing the formation of the β-structure that stabilises amyloid fibrils and can influence elongation (44) and inhibitors have been described that specifically inhibit secondary nucleation (20), but the impact of these interventions on residual Aβ monomer concentration has not always been described. The kinetic theory of protein aggregation inhibition reveals that inhibitors such as those described here, which sequester monomeric Aβ42, will reduce the rates of primary nucleation, elongation and secondary nucleation, and are therefore likely to have a large impact on amyloid assembly overall (45).

In AD, where certain oligomeric forms have been shown to impact neuronal function or cause cytotoxicity, the sequestration of monomer into non-toxic assemblies and consequent reduction of oligomer formation, could be beneficial. The intrinsically disordered and dynamic nature of monomeric Aβ42 has impeded the use of traditional approaches that focus on identifying chemical moieties that bind to defined sites on the target. Recently a small molecule (10074-G5) that binds to the monomeric form of Aβ42 has been reported (45, 46).The binding of 10074-G5 to Aβ42, with K_D of ~40 µM, increases the conformational entropy of the Aβ42 monomer while reducing the hydrophobicity of the protein. The binding of 10074-G5 sequesters Aβ42 in its soluble form and the binding of the molecule affects some conformations in the ensemble of monomeric Aβ42. This is reflected in a change in solvent exchange profile when 10074-G5 is added to Aβ42 at a 2:1 molar ratio. In contrast, here we observed an immediate uniform reduction in signal intensity across the spectrum when **C16** was added to Aβ42 at a 1:1 ratio, indicating that **C16** sequesters Aβ42 in a polymeric, insoluble assembly. The small molecule 10074-G5 reduces functional deficits in a *C. elegans* model of Aβ42-associated toxicity, however the impact of this small molecule on the population of cytotoxic Aβ42 oligomers and neuronal toxicity is yet to be reported. Thus further work is required to define the relative benefit of Aβ42 sequestration in monomeric versus non-toxic oligomeric form.

The inventive modular design of the compounds described here, built on a cyclam scaffold, a variable number of pendant groups easily introduced using 'click' chemistry, and the potential for coordinating different metal ions, offer a toolkit for future modification and the rational design of inhibitors of protein aggregation. This class of compounds can provide wide mass-to-charge and hydrophobic-to-hydrophilic surface area ratios, while the attachment of both rigid and flexible pendants provides a great diversity of possible interactions with client protein targets. The switchable geometry allows maintenance of a constant periphery while varying the gross molecular shape. Given that self-assembly and aggregation of proteins are three-dimensional processes, this level of structural control has significant potential to contribute to effective inhibition. Compounds that were effective at Aβ42 monomer sequestration protected against Aβ42-induced cytotoxicity. The modular scaffold design of these inhibitors provides a base for future rational design of more potent compounds that act through the same mechanism. AD is one of over 50 human disorders that are considered to be proteinopathies. The critical pathogenic species associated with protein aggregation and amyloid formation in each of these disorders will likely have unique features. A similar dissection of assembly pathways with rationally designed modulators may reveal points for therapeutic intervention in other protein aggregation-related diseases for which there are currently few effective therapies.

Materials and Methods

Synthesis of lead compounds C16–C18.

Full synthetic procedures and characterisation data are detailed in the Supporting Information.

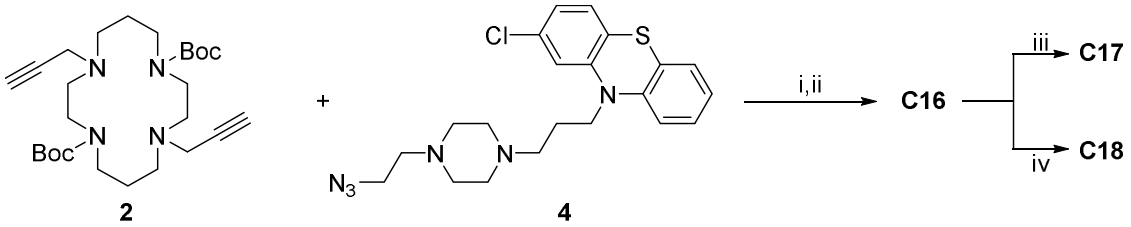

Reaction scheme 1: Cyclam (1,4,8,11-tetraazacyclotetradecane) **1** was converted to the di-Boc-di-propargyl derivative **2** in 68% yield over four steps using previously reported methods (47, 48). Perphenazine **3** was converted to the azide **4** (79%) by activating its primary alcohol with diphenylphosphoryl azide (DPPA) and displacing with sodium azide in dimethylformamide (DMF). The azide **4** (2 equivalents) and bis-alkyne **2** were coupled using a copper-catalysed azide/alkyne cycloaddition reaction (CuAAC) to yield the protected ligand **5** (46%), before the Boc groups were removed using 4M HCl in dioxane to afford **C16** (74%). The HCl salt **C16** was converted to its zinc(II) (**C17**) and copper(II) (**C18**) complexes by first treating with Ambersep 900 hydroxide form resin to generate the free amine, then stirring overnight at room temperature with either zinc(II) perchlorate hexahydrate (for **C17**, 63%) or copper(II) perchlorate hexahydrate (for **C17**, 64%). All compounds were dissolved in 100% DMSO and stored at 4 °C until use. Reagents and conditions: i. $CuSO_4.5H_2O$ (0.2 equiv.), sodium ascorbate (0.5 equiv.), THF/H_2O (2:3), rt, 16 h, 46%; ii. 4M HCl in dioxane (excess), 0 °C, 1 h, 74%; iii. Ambersep 900 hydroxide form resin, MeOH, 15 min, then $Zn(ClO_4)_2$, MeOH, reflux, 16 h, 63%; iv. Ambersep 900 hydroxide form resin, MeOH, 15 min, then $Cu(ClO_4)_2$, MeOH, reflux, 16 h, 64%.

Aβ42 Overexpression. Overexpression and purification of Aβ42 was performed according to Walsh and colleagues with slight modifications (34). A modified pET plasmid (100–300 ng) encoding the Aβ(M1–42) gene was transformed into *E.coli* BL21-Gold (DE3) competent cells. A single colony from an *E.coli* BL21-Gold (DE3) transformation plate was used to inoculate 100 mL LB medium containing 100 µg/mL AMP. This culture was incubated at 37 °C overnight with shaking (180 rpm) and then used to inoculate fresh LB media containing 100 µg/mL AMP (1000 mL) to reach a starting optical density of 0.05 at 600 nm (OD600). Large cultures were incubated at 37 °C with shaking (180 rpm) until the cell density reached OD600 of 0.7–0.9, when expression was induced with addition of 0.5 mM IPTG.

Cultures were incubated for a further 3 h and then cells harvested by centrifugation at ~7500 x g for 30 min at 10 °C. Cells were resuspended into 25 mL 10 mM Tris/HCl pH 8.0, 1 mM EDTA and stored at –20 °C. Samples of pre-induction and post-induction cultures (5 mL) were centrifuged at ~3300 x *g* for 10 min at 4 °C and the cell pellet resuspended in BugBuster® reagent with DNase I. Samples were sonicated 3 x 30 s with 30 s rest on ice between each sonication. Soluble and insoluble fractions were separated by centrifugation at 16000 x *g* for 5 min and the insoluble material resuspended in an equivalent volume of urea buffer. Expression was analysed using Novex™ 10–20% Tricine SDS-PAGE gels, stained with Coomassie Blue.

^{15}N Aβ42 was expression was performed according to Habchi and colleagues (20). A single colony from an *E. coli* BL21-Gold (DE3) transformation plate was used to inoculate 200 mL LB medium containing 100 µg/mL AMP. This culture was incubated at 37 °C overnight with shaking (180 rpm) and then used to inoculate 4L 2XYT media (1/25 dilution) containing 100 µg/mL AMP. Cultures were incubated at 37 °C with shaking (180 rpm) until the cell density reached OD600 of 0.5. Cells harvested by centrifugation at ~7500 x g for 20 min at 10 °C. Cells were washed with M9 and resuspended in 1 L (1/4 of initial culture volume) of minimal M9 medium containing 100 µg/mL AMP and 2g/L $^{15}NH_4Cl$. Cultures were incubated at 37 °C with shaking (180 rpm) for 2 h and expression was induced with addition of 1 mM IPTG. Cells were grown overnight and harvested by centrifugation at 7446 x *g* for 30 min at 10 °C. Cells were resuspended into 25 mL of 10 mM Tris/HCl pH 8.0, 1 mM EDTA and stored at –20 °C.

Aβ42 Purification and Concentration. Frozen cell pellets from 4 L culture were thawed, mixed by vortex, sonicated for 2 min (1/2" horn, 50% duty cycle) and then centrifuged for 10 min at 18000 x *g*. The supernatant was removed and the pellet was resuspended in 100 mL 10 mM Tris/HCl pH 8.0, 1 mM EDTA, then sonicated 15 s (1/2" horn, 50% duty cycle) and centrifuged as above. This step was performed twice. After the third supernatant was removed, the pellet was resuspended and sonicated 90 s (1/2" horn, 50% duty cycle) in 150 mL of fresh ice cold deionised 8 M urea, 20 mM Tris/HCl pH 8.0, 1 mM EDTA, resulting in a clear solution.

50 mL of diethylaminoethyl (DEAE) cellulose beads were pre-incubated with 2 M urea, 10 mM Tris/HCl pH 8.0, 1 mM EDTA. 100 mL of the urea-solubilised inclusion bodies was diluted with 300 mL of 10 mM Tris/HCl pH 8.0, 1 mM EDTA and added to the DEAE-cellulose beads in a glass beaker on ice. This slurry was stirred gently every 5 min for a total of 30 min, then filtered under vacuum using a Büchner funnel with filter paper and the flowthrough collected. Beads were washed with 100 mL of 10 mM Tris/HCl pH 8.0, 1 mM EDTA and the protein eluted using twelve 50 mL-volumes of 10 mM Tris/HCl pH 8.0, 1 mM EDTA, supplemented with increasing concentrations of NaCl (1 x 25 mM, 8 x 150 mM, 1 x 250 mM and 2 x 500 mM). Samples from fractions were analysed for Aβ42 content by Novex™ 10–20% Tricine SDS-PAGE gels.

Fractions containing elevated levels of Aβ42 were combined and filtered through a 30 kDa molecular mass cut-off centrifugal filtration device (Amicon® Ultra-15). The combined sample was concentrated from 400 mL to 30 mL using a 3 kDa molecular mass cut-off centrifugal filtration device (Amicon® Ultra-15). The concentrated sample was aliquoted into 2.5 mL tubes, snap frozen using liquid nitrogen and then lyophilised. Lyophilised aliquots were stored at –20 °C.

Size exclusion chromatography. An aliquot of lyophilised Aβ42 protein was solubilised in 500 µL of 6 M GuHCl until no large aggregates were visible. This sample was centrifuged at ~3300 x *g* for 3 min, bath sonicated for 5 min in ice water and centrifuged again at 16000 x *g* for 10 min at 4 °C. 500 µL of sample was drawn up carefully with a syringe so as to not disturb the pelleted aggregated protein and loaded onto a Superdex™ 75 Increase 10/300 GL size exclusion column running on an ÄKTA FPLC system. Protein was eluted at 0.5 ml/min in 50 mM ammonium acetate pH 8.5. Fractions (0.5 mL) were collected in Protein LoBind Eppendorf tubes and immediately placed on ice. Fractions were analysed for Aβ42 content using SDS-PAGE. Concentration was measured via

spectrophotometer (ε275 = 1450). Fractions containing Aβ42 were combined and either used immediately or snap frozen and lyophilised.

Thioflavin T assays. Protein samples (Aβ42) were prepared in triplicate in non-binding 96-well half area plates (Corning 3881) in 25 mM or 50 mM NaH_2PO_4 pH 7.4, 40 µM ThT to a final volume of 80 µL. Plate preparation was performed at 4 °C to minimise aggregation. Samples incubated at 37 °C in a POLARstar Omega microplate reader (BMG Labtech), with excitation at 440 nm and the fluorescence emission recorded at 480 nm under quiescent conditions.

Seeding. Seeds were made by incubating 10 µM Aβ42 in 50 mM NaH_2PO_4, pH 7.4 at 37 °C for 5 h. Protein solution was subject to 6 x 10 s sonication with 20 s rest on ice in between each interval. The seeds were kept on ice and used immediately.

Enhanced BCA assay details. Kinetic assays were ran to completion as judged by the plateau in ThT fluorescence (~5 hours). Contents of wells were removed and centrifuged at 16000 x g for 10 min to pellet fibrils and aggregates. Protein concentration was determined using a Pierce® Bicinchoninic Acid Protein Assay Kit according to manufacturer's enhanced protocol. Monomeric Aβ42 and compounds alone were used as controls.

TEM. Samples were prepared on carbon-coated copper grids (200 mesh) with formvar support film (ProSciTech Pty Ltd.) that were exposed to UV light (230 nm) for 10 min before sample application and stained with 2% aqueous uranyl acetate solution. Samples were examined with a FEI Tecnai T12 electron microscope operating at 120 kV and images captured with a Veleta CCD camera and processed using RADIUS 2.0 imaging software (EMSIS GmbH).

Preparation of Aβ42 for cell assay and NMR. Freeze dried purified protein was resuspended in HFIP at 1 mg/ml and incubated for 30 min at room temperature. Protein was snap frozen, lyophilised, and stored at –80 °C until use.

Cell Culture and Differentiation. SH-SY5Y cells were cultured in in Dulbecco's Modified Eagle Medium: Nutrient Mixture F-12 (DMEM/F12; Invitrogen, Carlsbad, CA, USA) supplemented with 10% fetal bovine serum (FBS; Gibco, Uxbridge, UK) at 37˚C and 5% CO2. Cells were fed every 2-3 days and passaged using Trypsin-EDTA (0.25%). Cells were detached using Trypsin-EDTA, centrifuged (5 min, 125 x *g*), counted and then plated in a Cell-bind 96-well plate at a density of $0.5x10^4$ cells/well in 10 µM all-trans retinoic acid (RA; Sigma-Aldrich) in DMEM/F12 with 10% FBS. Media was replaced daily for 4 days (RA is light sensitive, so all steps involving RA were completed in the dark). After a 4-day incubation with RA, media was switched to DMEM/F12 (no serum) with 50 ng/ml BDNF (Sigma-Aldrich) for 3 days. After a total of 7 days of differentiation the cells were used for the experiments.

Aβ42 preparation, compound treatment and CellTiter-Blue® viability assay. 24 h prior to the cells finishing differentiation an aliquot of Aβ42 was centrifuged at 16,000 x *g* for 10 min and dissolved in PBS at 200 µM, then diluted to 20 µM in DMEM/F12 with 10% FBS. The solution was stored in the incubator (37 °C, 5% CO_2) in a low-bind Eppendorf to promote Aβ42 fibrillization. After cell differentiation was complete, for the Aβ42 monomeric preparation, a second aliquot of Aβ42 was centrifuged at 16,000 x *g* for 10 min, dissolved in PBS at 200 µM and immediately diluted to a final concentration of 20 µM in DMEM/F12 (with 10% FBS). Experimental compounds (10 µM, 0.1%) or DMSO control were added to the fibrillar or monomeric Aβ42. Differentiation media was aspirated, 100 µL of each condition added to the cells and incubated for 24 hours (37 °C, 5% CO_2). In the monomeric preparation, the time between dissolving the Aβ42 and applying onto the cells was minimised (less than 2 minutes total). After 24 h, CellTiter-Blue® (CTB; Promega G8080) (20 µl/well) was added and incubated for 4 h. The fluorescent emission at 590 nm was measured using a POLARstar Omega microplate-reader (BMG Labtech); viable cells metabolise this agent and reduce it to a fluorescent compound.

Statistical Analysis. One-way ANOVA (analysis of variance) followed by a Bonferroni's multiple comparisons test was used to determine the differences between mean CTB values of differentiated

SH-SY5Y cells treated with Aβ42 and/or test compounds relative to vehicle control. Significance threshold was defined as $p < 0.05$.

Kinetic analysis. The kinetic data obtained in ThT assays were analysed using the online fitting software AmyloFit, following the referred protocol (41). The model 'secondary nucleation dominated, unseeded' was used, with the reaction orders set to 2 as typical for Aβ42 and under the constraint of allowing deviations from the unperturbed kinetics in only one parameter at a time to investigate which microscopic step or which species of the aggregation mixture was most likely affected by the inhibitors. Repeats of the experiment were analysed separately and combined at the end to estimate uncertainty.

***K_d* determination** To determine the value of the dissociation constant, K_d, between free monomer and inhibitor, a one-to-one binding was assumed and the free monomer concentration, m, expressed as a function of the total inhibitor concentration, I_{tot}, the total monomer concentration, m_{tot}, and K_d,

$m = \frac{-I_{tot}+m_{tot}-K_d+\sqrt{(I_{tot}-m_{tot}+K_d)^2+4\,K_d\,m_{tot}}}{2}$. The free monomer concentration was estimated as the effective monomer concentration in the kinetic assays or the relative one-dimensional 1H NMR signal, respectively. Likelihoods were calculated using grid approximations, under the assumption of Gaussian noise.

NMR / K_d Analysis. All NMR data was collected at 4 °C using unlabelled 10 μM Aβ42 or ^{15}N-labelled Aβ42 in 20 mM NaH_2PO_4 pH 7.0, 10% D2O, 1 mM DSS. Individual titrations with C16, C17, C18 and EGCG were carried out by incubating unlabelled 10 μM Aβ42 with increasing concentrations of the compounds, ranging from 0 to 50 μM. 9 titration points were recorded for each compound. The NMR signal from one-dimensional ^{1}H spectra was used to monitor the binding. Each spectrum was recorded using 512 scans. A ^{1}H-^{15}N heteronuclear single quantum coherence (HSQC) spectrum was also recorded for ^{15}N-labelled Aβ42 in the presence of 10 μM C16. The HSQC was recorded overnight, for 240 scans, with a spectral width of 25 ppm (^{15}N offset at 117.5 ppm). All spectra were obtained using a 18.8 T (800 MHz ^{1}H frequency) Advance III HD Bruker spectrometer equipped with a cryoprobe.

Acknowledgements

The work was funded by Australian Research Council Discovery Project grant (DP200102463) to MS, AK and PJR. SRB, JSPA and MAS were supported by a Research Training Program Scholarship from the Australian Government (Department of Education, Skills and Employment). MK, MAS and ELW's research is supported by the National Health and Medical Research Council of Australia (NHMRC; APP1132524). MK is an NHMRC Principal Research Fellow (APP1154692). MRZ acknowledges support from the Herchel Smith Fund. The authors thank Elva (Meng) Shi and Dr Malcolm Spain for assistance with synthesis and characterisation of compounds and Dr Bill Bubb for comments on the manuscript. The authors acknowledge the facilities and the scientific and technical assistance of staff within the Sydney Analytical and Sydney Microscopy & Microanalysis Core Research Facilities at the University of Sydney. We acknowledge and pay respect to the Gadigal people of the Eora Nation, the traditional owners of the land on which we research, teach, and collaborate at the University of Sydney.

References

1. Gillam JE & MacPhee CE (2013) Modelling amyloid fibril formation kinetics: mechanisms of nucleation and growth. *Journal of physics. Condensed matter : an Institute of Physics journal* 25(37):373101.
2. Nelson R, *et al.* (2005) Structure of the cross-beta spine of amyloid-like fibrils. *Nature* 435(7043):773-778.

3. Sunde M & Blake C (1997) The structure of amyloid fibrils by electron microscopy and X-ray diffraction. *Advances in protein chemistry* 50:123-159.
4. Bjorkli C, Sandvig A, & Sandvig I (2020) Bridging the Gap Between Fluid Biomarkers for Alzheimer's Disease, Model Systems, and Patients. *Front Aging Neurosci.* 12:272. 10.3389/fnagi.2020.00272.
5. Benilova I, Karran E, & De Strooper B (2012) The toxic Aβ oligomer and Alzheimer's disease: an emperor in need of clothes. *Nature neuroscience* 15(3):349-357.
6. Lee SJC, Nam E, Lee HJ, Savelieff MG, & Lim MH (2017) Towards an understanding of amyloid-β oligomers: characterization, toxicity mechanisms, and inhibitors. *Chemical Society Reviews* 46(2):310-323.
7. Walsh DM*, et al.* (2002) Naturally secreted oligomers of amyloid beta protein potently inhibit hippocampal long-term potentiation in vivo. *Nature* 416(6880):535-539.
8. Chiti F & Dobson CM (2009) Amyloid formation by globular proteins under native conditions. *Nature chemical biology* 5(1):15-22.
9. Fantini J, Chahinian H, & Yahi N (2020) Progress toward Alzheimer's disease treatment: Leveraging the Achilles' heel of Aβ oligomers? *Protein Science* 29(8):1748-1759.
10. Jadiya P*, et al.* (2019) Impaired mitochondrial calcium efflux contributes to disease progression in models of Alzheimer's disease. *Nature communications* 10(1):3885.
11. Tsigelny IF*, et al.* (2014) Structural diversity of Alzheimer's disease amyloid-β dimers and their role in oligomerization and fibril formation. *Journal of Alzheimer's disease : JAD* 39(3):583-600.
12. Tsigelny IF*, et al.* (2012) Role of α-synuclein penetration into the membrane in the mechanisms of oligomer pore formation. *The FEBS journal* 279(6):1000-1013.
13. Winner B*, et al.* (2011) In vivo demonstration that α-synuclein oligomers are toxic. *Proceedings of the National Academy of Sciences* 108(10):4194-4199.
14. Zott B*, et al.* (2019) A vicious cycle of β amyloid–dependent neuronal hyperactivation. *Science* 365(6453):559-565.
15. Törnquist M*, et al.* (2020) Ultrastructural evidence for self-replication of Alzheimer-associated Aβ42 amyloid along the sides of fibrils. *Proceedings of the National Academy of Sciences* 117(21):11265-11273.
16. Cohen SIA*, et al.* (2013) Proliferation of amyloid-β42 aggregates occurs through a secondary nucleation mechanism. *Proceedings of the National Academy of Sciences* 110(24):9758-9763.
17. Michaels TCT*, et al.* (2020) Dynamics of oligomer populations formed during the aggregation of Alzheimer's Aβ42 peptide. *Nature Chemistry* 12(5):445-451.
18. Serra-Batiste M*, et al.* (2016) Aβ42 assembles into specific β-barrel pore-forming oligomers in membrane-mimicking environments. *Proceedings of the National Academy of Sciences* 113(39):10866-10871.
19. Habchi J*, et al.* (2016) An anticancer drug suppresses the primary nucleation reaction that initiates the production of the toxic Aβ42 aggregates linked with Alzheimer's disease. *Science Advances* 2(2):e1501244.
20. Habchi J*, et al.* (2017) Systematic development of small molecules to inhibit specific microscopic steps of Aβ42 aggregation in Alzheimer's disease. *Proceedings of the National Academy of Sciences* 114(2):E200-E208.
21. Limbocker R*, et al.* (2019) Trodusquemine enhances Aβ42 aggregation but suppresses its toxicity by displacing oligomers from cell membranes. *Nature communications* 10(1):225.
22. Bieschke J*, et al.* (2010) EGCG remodels mature α-synuclein and amyloid-β fibrils and reduces cellular toxicity. *Proceedings of the National Academy of Sciences* 107(17):7710-7715.
23. Du W-J*, et al.* (2015) Brazilin inhibits amyloid β-protein fibrillogenesis, remodels amyloid fibrils and reduces amyloid cytotoxicity. *Scientific Reports* 5(1):7992.
24. Ehrnhoefer DE*, et al.* (2008) EGCG redirects amyloidogenic polypeptides into unstructured, off-pathway oligomers. *Nature Structural & Molecular Biology* 15(6):558-566.
25. Palhano FL, Lee J, Grimster NP, & Kelly JW (2013) Toward the molecular mechanism(s) by which EGCG treatment remodels mature amyloid fibrils. *Journal of the American Chemical Society* 135(20):7503-7510.
26. Ettcheto M*, et al.* (2020) Epigallocatechin-3-Gallate (EGCG) Improves Cognitive Deficits Aggravated by an Obesogenic Diet Through Modulation of Unfolded Protein Response in APPswe/PS1dE9 Mice. *Molecular neurobiology* 57(4):1814-1827.

27. Tamanini E, *et al.* (2010) Cyclam-Based "Clickates": Homogeneous and Heterogeneous Fluorescent Sensors for Zn(II). *Inorganic Chemistry* 49(8):3789-3800.
28. Wong JK-H, *et al.* (2016) Synthesis and Evaluation of 1,8-Disubstituted-Cyclam/Naphthalimide Conjugates as Probes for Metal Ions. *ChemistryOpen* 5(4):375-385.
29. Yu M, *et al.* (2014) Neuroprotective peptide–macrocycle conjugates reveal complex structure–activity relationships in their interactions with amyloid β. *Metallomics* 6(10):1931-1940.
30. Zhu L, Song Y, Cheng P-N, & Moore JS (2015) Molecular Design for Dual Modulation Effect of Amyloid Protein Aggregation. *Journal of the American Chemical Society* 137(25):8062-8068.
31. Meisl G, *et al.* (2014) Differences in nucleation behavior underlie the contrasting aggregation kinetics of the Aβ40 and Aβ42 peptides. *Proceedings of the National Academy of Sciences* 111(26):9384-9389.
32. Risacher SL, *et al.* (2019) Plasma amyloid beta levels are associated with cerebral amyloid and tau deposition. *Alzheimer's & dementia (Amsterdam, Netherlands)* 11:510-519.
33. Linse S (2020) Expression and Purification of Intrinsically Disordered Aβ Peptide and Setup of Reproducible Aggregation Kinetics Experiment. *Methods in molecular biology (Clifton, N.J.)* 2141:731-754.
34. Walsh DM, *et al.* (2009) A facile method for expression and purification of the Alzheimer's disease-associated amyloid beta-peptide. *The FEBS journal* 276(5):1266-1281.
35. House E, *et al.* (2004) Aluminium, iron, zinc and copper influence the in vitro formation of amyloid fibrils of Abeta42 in a manner which may have consequences for metal chelation therapy in Alzheimer's disease. *Journal of Alzheimer's disease : JAD* 6(3):291-301.
36. Lee M-C, *et al.* (2018) Zinc ion rapidly induces toxic, off-pathway amyloid-β oligomers distinct from amyloid-β derived diffusible ligands in Alzheimer's disease. *Scientific Reports* 8(1):4772.
37. Mold M, Ouro-Gnao L, Wieckowski BM, & Exley C (2013) Copper prevents amyloid-β1–42 from forming amyloid fibrils under near-physiological conditions in vitro. *Scientific Reports* 3(1):1256.
38. Krishtal J, Bragina O, Metsla K, Palumaa P, & Tõugu V (2017) In situ fibrillizing amyloid-beta 1-42 induces neurite degeneration and apoptosis of differentiated SH-SY5Y cells. *PLOS ONE* 12(10):e0186636.
39. Cohen SI, *et al.* (2011) Nucleated polymerization with secondary pathways. I. Time evolution of the principal moments. *The Journal of chemical physics* 135(6):065105.
40. Knowles TPJ, *et al.* (2009) An Analytical Solution to the Kinetics of Breakable Filament Assembly. *Science* 326(5959):1533-1537.
41. Meisl G, *et al.* (2016) Molecular mechanisms of protein aggregation from global fitting of kinetic models. *Nature protocols* 11(2):252-272.
42. Lopez del Amo JM, *et al.* (2012) Structural properties of EGCG-induced, nontoxic Alzheimer's disease Aβ oligomers. *Journal of molecular biology* 421(4-5):517-524.
43. Roche J, Shen Y, Lee JH, Ying J, & Bax A (2016) Monomeric Aβ(1-40) and Aβ(1-42) Peptides in Solution Adopt Very Similar Ramachandran Map Distributions That Closely Resemble Random Coil. *Biochemistry* 55(5):762-775.
44. Horsley JR, *et al.* (2020) Rationally designed peptide-based inhibitor of Aβ42 fibril formation and toxicity: a potential therapeutic strategy for Alzheimer's disease. *The Biochemical journal* 477(11):2039-2054.
45. Michaels TCT, *et al.* (2020) Thermodynamic and kinetic design principles for amyloid-aggregation inhibitors. *Proceedings of the National Academy of Sciences*:202006684.
46. Heller GT, *et al.* (2020) Small-molecule sequestration of amyloid-β as a drug discovery strategy for Alzheimer's disease. *Science Advances* 6(45):eabb5924.
47. Spain M, *et al.* (2018) Antitubercular Bis-Substituted Cyclam Derivatives: Structure–Activity Relationships and in Vivo Studies. *Journal of Medicinal Chemistry* 61(8):3595-3608.
48. Yu M, Yu Q, Rutledge PJ, & Todd MH (2013) A Fluorescent "Allosteric Scorpionand" Complex Visualizes a Biological Recognition Event. *ChemBioChem* 14(2):224-229.

Figures

Fig 1. *(A)* Schematic illustration of the multi-step process of Aβ42 amyloid assembly. *(B)* The lead compounds used in this study combine a cyclam macrocycle (purple) with pendant perphenazine moieties (cyan), conjugated via a click-derived triazole, and deployed either as the unmetallated HCl salt **C16**, the zinc perchlorate complex **C17**, or the copper(II) perchlorate **C18**. Other compounds screened in the initial phase of the project have a similar overall structure, bearing naphthyl- (**C10**–**C12**) or dopamine- (**C13**–**C15**) derived pendants in place of the perphenazine portion, as well as 'single-armed' compounds that contain only one triazolyl-pendant group (and a third secondary amine N–H at the other position on the macrocycle), **C1**–**C9**. Structures for all compounds are shown in Figure S1 of the Supporting Information.

Fig. 2. Time courses of fibril formation by Aβ42 show concentration-dependent inhibition of aggregation by **C16**, **C17** and **C18**. *(A)* 10 μM monomeric Aβ42 in the absence or presence of either 1% DMSO (dark grey) or 10 – 50 μM of **C16** (pink), **C17** (blue) and **C18** (green). Lower section displays an enlarged 10-hour window. N = 3 (SI Fig S3). *(B)* 2.5 μM monomeric Aβ42 in the presence of either 1% DMSO (dark grey) or 0.1, 1, 2, 3 or 5 μM of compounds. N = 4 (SI Fig S4). *(C)* Characterisation of the effects of compounds on seeded Aβ42 aggregation. 10 μM monomeric Aβ42 with 2% seeds in the absence or presence of either 1% DMSO (dark grey), 25 or 50 μM of compounds. Unseeded data are shown in pale colours for comparison. N = 3 (SI Figs S15). All samples were measured in triplicate under quiescent conditions at 37 °C. Traces have been corrected for time zero and data normalised as a function of the maximum fluorescence intensity, using GraphPad Prism.

Fig. 3. Transmission electron microscopy images showing representative examples of the morphology of fibrils formed by 10 μM Aβ42 alone (A) or aggregates formed by 10 μM Aβ42 in the presence of 50 μM **C16** (B), **C17** (C) and **C18** (D). Scale bar represents 200 nm.

Fig. 4. Cell viability was measured using the CellTiter Blue® assay after 24 h incubation with vehicle or 10 μM compound, with or without 20 μM Aβ42. *(A)* Compounds alone. *(B)* Compounds incubated with monomeric Aβ42. *(C)* Compounds incubated with fibrillar Aβ42. The figure displays the mean ± SD of N ≥ 3 independent experiments. One-way ANOVA followed by a Bonferroni's multiple comparisons test at the 0.05 level was used to determine the difference between each condition and vehicle control (**** $p < 0.0001$, *** $p < 0.001$, * $p < 0.05$, NS = non-significant). *(D)* Representative concentration-response curve for **C16** incubated with Aβ42 showing mean ± SD of duplicates. IC_{50} = 2.33 μM (SD = 0.89). N = 3.

Fig. 5. Chemical kinetics analysis reveals inhibition through monomer sequestration. To elucidate the major mechanism of inhibition, normalised aggregation curves measured in thioflavin T fluorescence assays were fitted under the constraint that deviation from the unperturbed system was allowed in only one microscopic step or the free monomer concentration, respectively. Representative curves shown in A and B, all fits shown in the SI. *(A)* The observed inhibition could not be described through inhibition of primary nucleation. *(B)* Inhibition through monomer sequestration was a plausible mechanism based on the kinetic profiles. *(C)* Microscopic steps underlying amyloid formation, with the suggested mode of inhibition through monomer sequestration. *(D)* Further support for monomer sequestration by **C16** was obtained through binding curves consistent with orthogonal NMR data, as well as a reasonable correlation between the effective free monomer concentration and the absolute increase in ThT signal over the experimental time course. *(E)* and *(F)* as in *(D),* but for **C17** and **C18**, respectively.

Fig. 6. One-dimensional ^{1}H NMR spectroscopy to determine apparent K_D for compounds. *(A)* Unlabelled 10 μM Aβ42 (dark grey) was incubated with 1–50 μM **C16** and spectra recorded at 4 °C. Methyl proton region is displayed, all regions analysed are shown in SI Fig. 16. *(B), (C)* and *(D)* as in *(A)* but for **C17**, **C18**, and **EGCG** respectively. Increasing concentration of **C16**–**C18** resulted in a decay in protein signal intensity. *(E)* Binding curve for **C16** constructed from signal decay curves and used to calculate the apparent K_D. *(F)* and *(G)* as in *(E)* but for **C17** and **C18**, respectively.

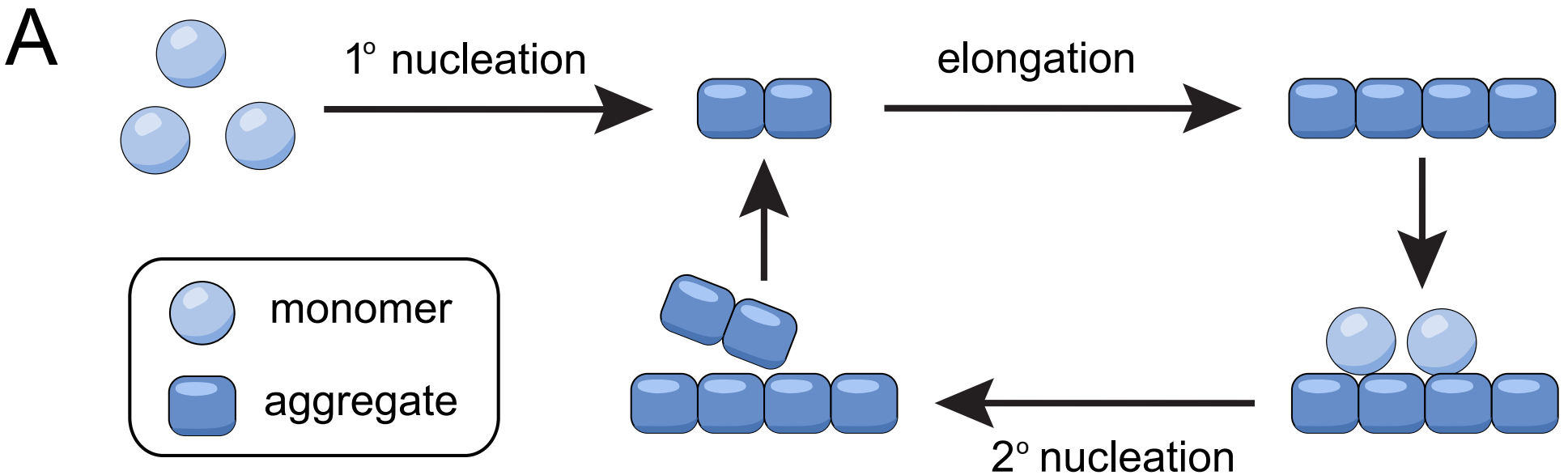

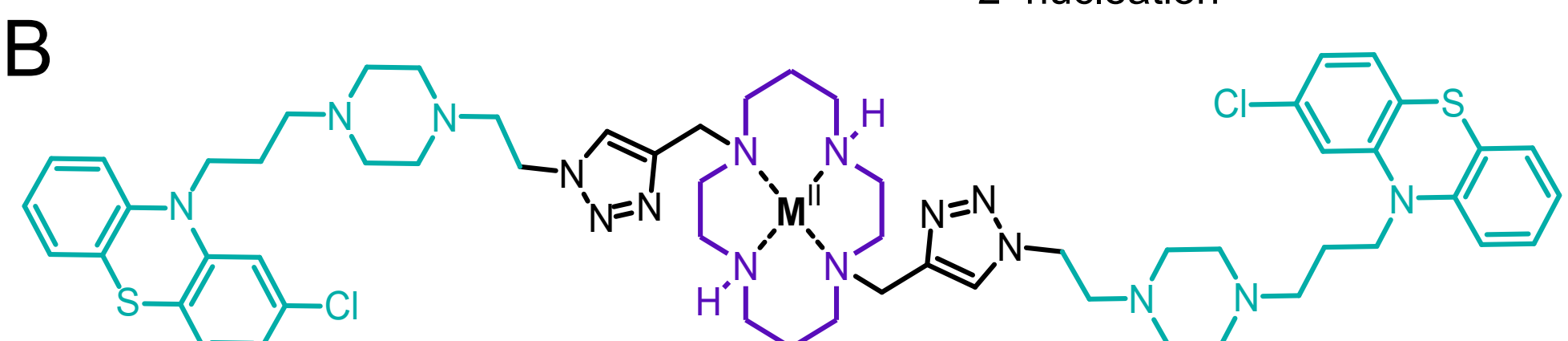

C16 M = none (as HCl salt)

C17 M = Zn (as $(ClO_4)_2$ salt)

C18 M = Cu (as $(ClO_4)_2$ salt)

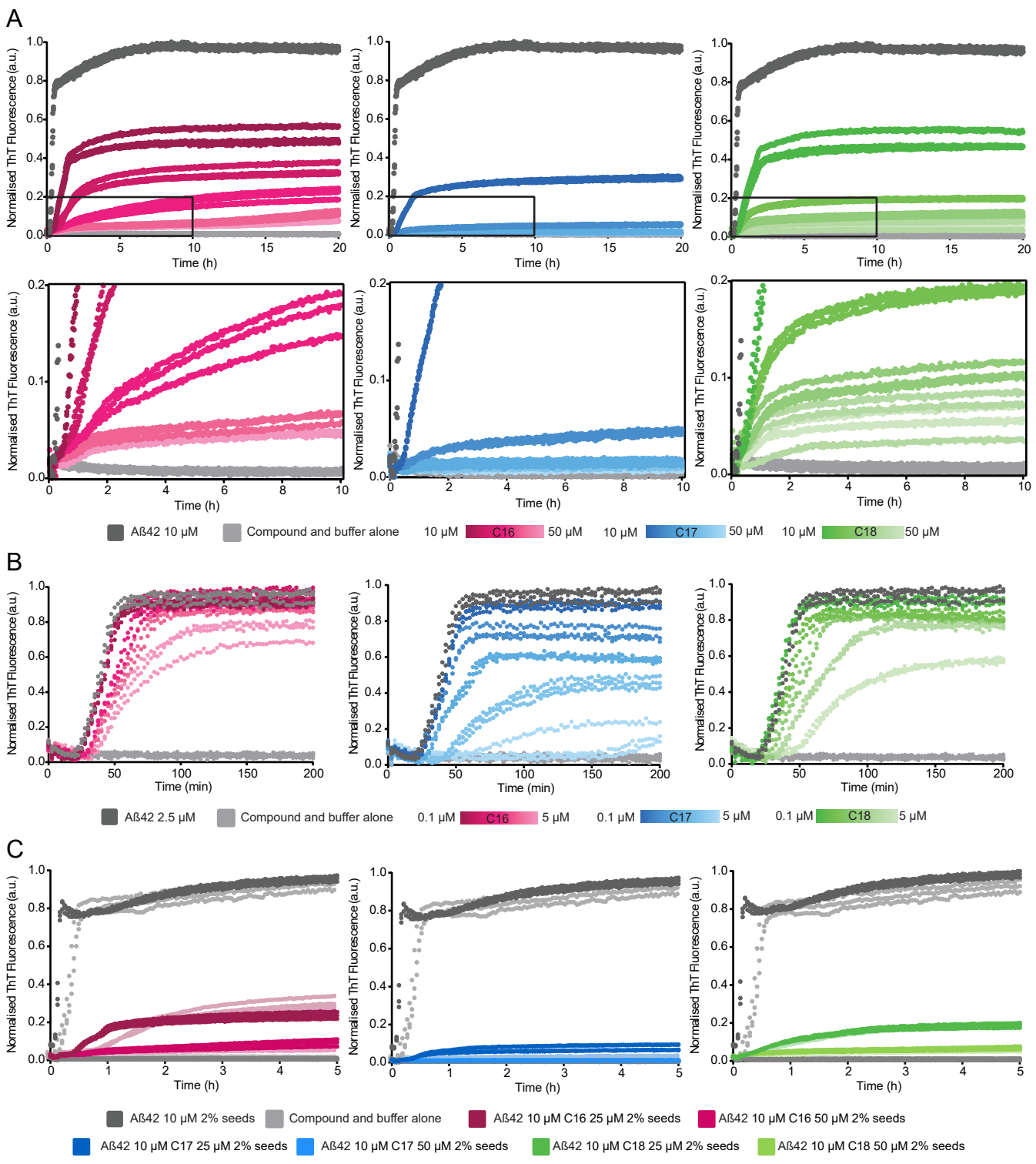
A
Normalised ThT Fluorescence (a.u.)
Time (h)
Aß42 10 µM
Compound and buffer alone
10 µM C16 50 µM
10 µM C17 50 µM
10 µM C18 50 µM
B
Time (min)
Aß42 2.5 µM
Compound and buffer alone
0.1 µM C16 5 µM
0.1 µM C17 5 µM
0.1 µM C18 5 µM
C
Aß42 10 µM 2% seeds
Compound and buffer alone
Aß42 10 µM C16 25 µM 2% seeds
Aß42 10 µM C16 50 µM 2% seeds
Aß42 10 µM C17 25 µM 2% seeds
Aß42 10 µM C17 50 µM 2% seeds
Aß42 10 µM C18 25 µM 2% seeds
Aß42 10 µM C18 50 µM 2% seeds

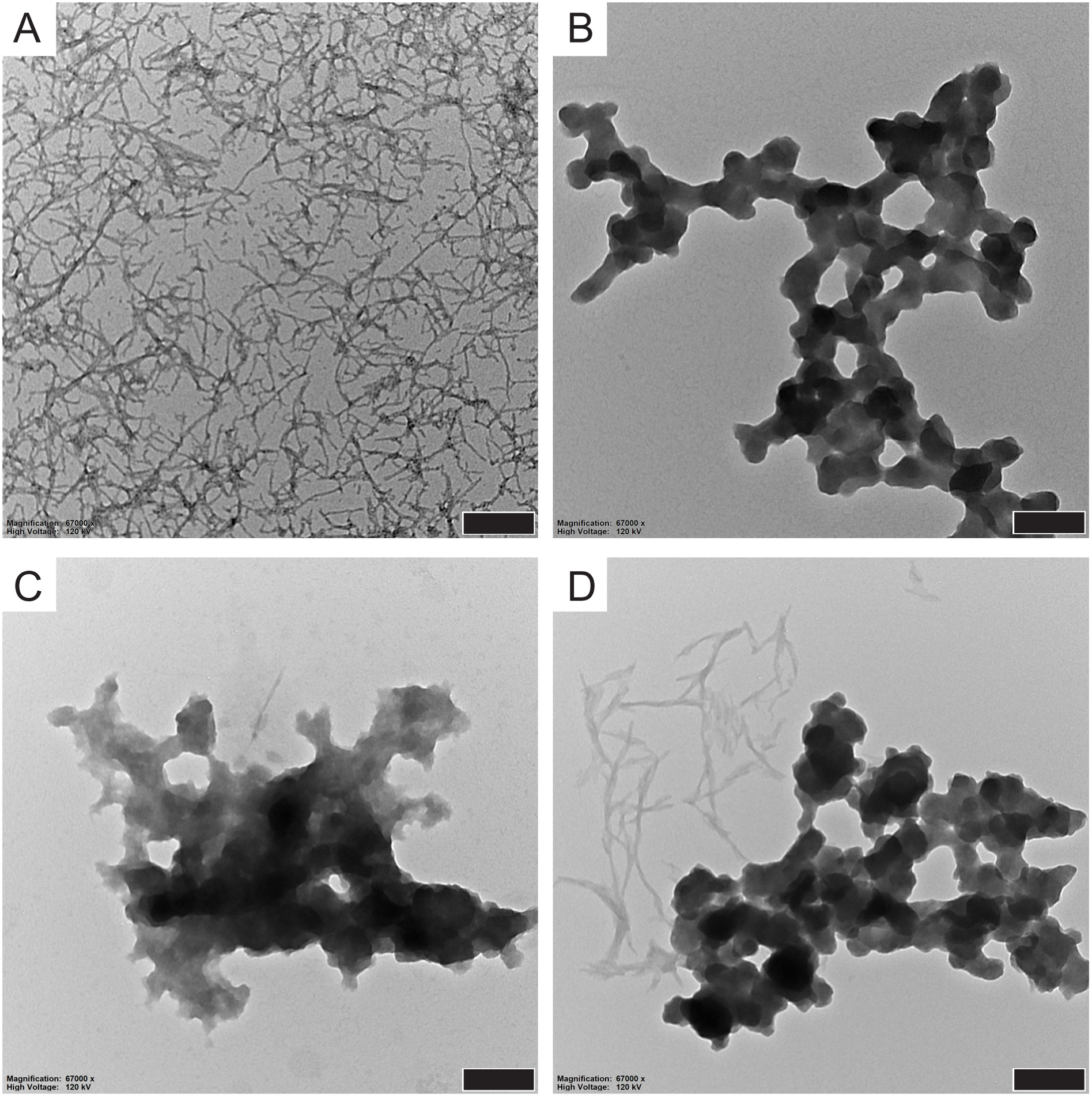
A
Magnification: 67000 x
High Voltage: 120 kV
B
Magnification: 67000 x
High Voltage: 120 kV
C
Magnification: 67000 x
High Voltage: 120 kV
D
Magnification: 67000 x
High Voltage: 120 kV

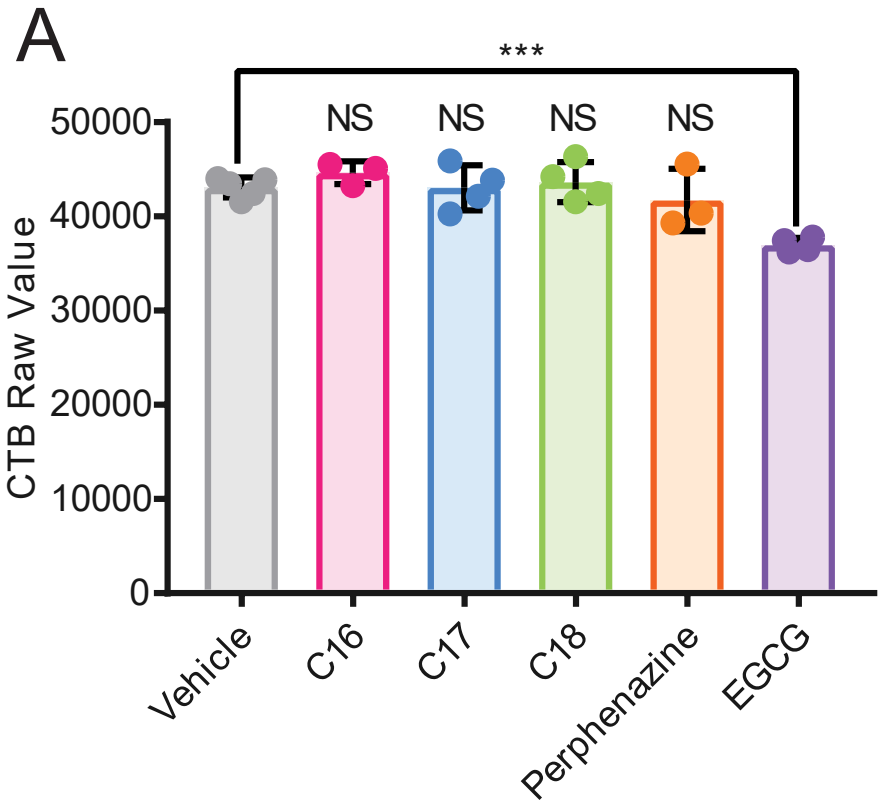
A
***
NS
NS
NS
NS
50000
40000
30000
20000
10000
0
CTB Raw Value
Vehicle
C16
C17
C18
Perphenazine
EGCG

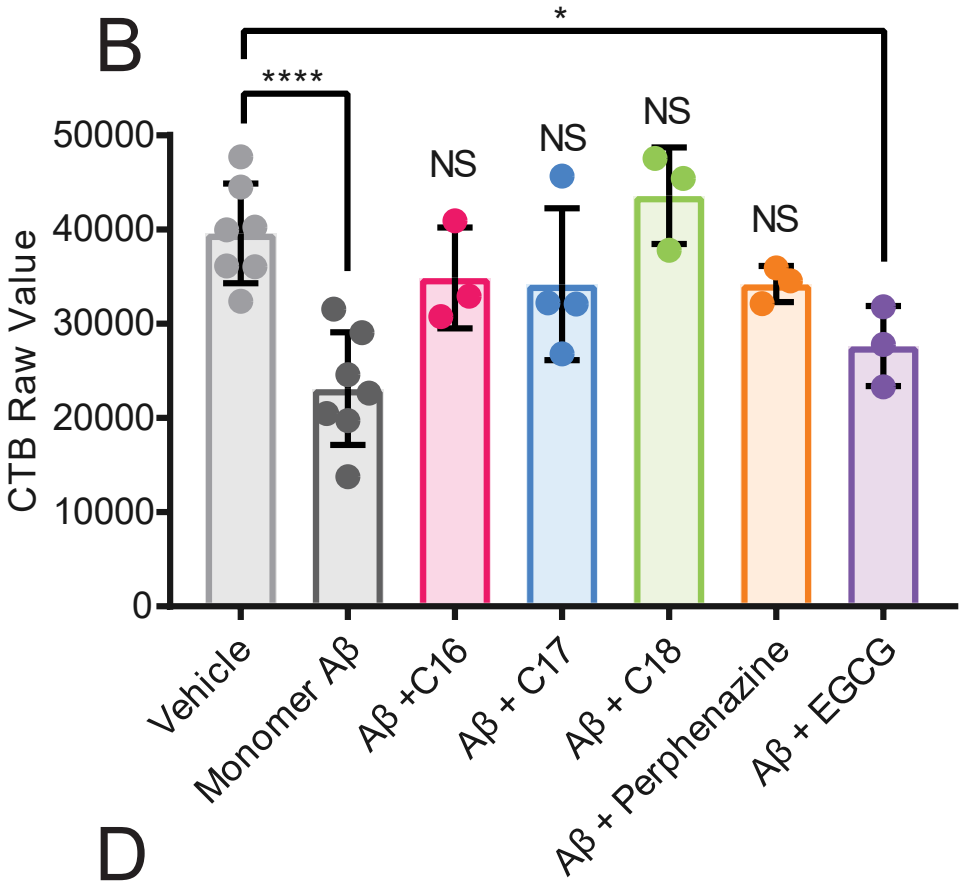
B
*
****
NS
NS
NS
NS
50000
40000
30000
20000
10000
0
CTB Raw Value
Vehicle
Monomer Aβ
Aβ +C16
Aβ + C17
Aβ + C18
Aβ + Perphenazine
Aβ + EGCG

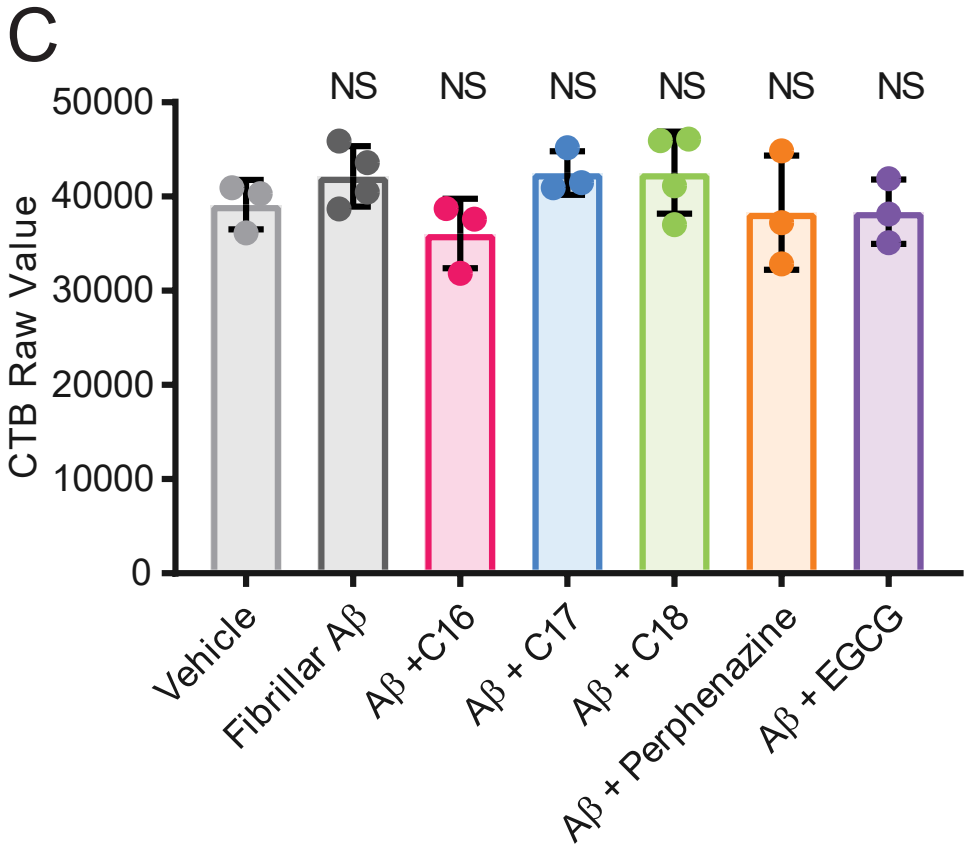
C
NS
NS
NS
NS
NS
NS
50000
40000
30000
20000
10000
0
CTB Raw Value
Vehicle
Fibrillar Aβ
Aβ +C16
Aβ + C17
Aβ + C18
Aβ + Perphenazine
Aβ + EGCG

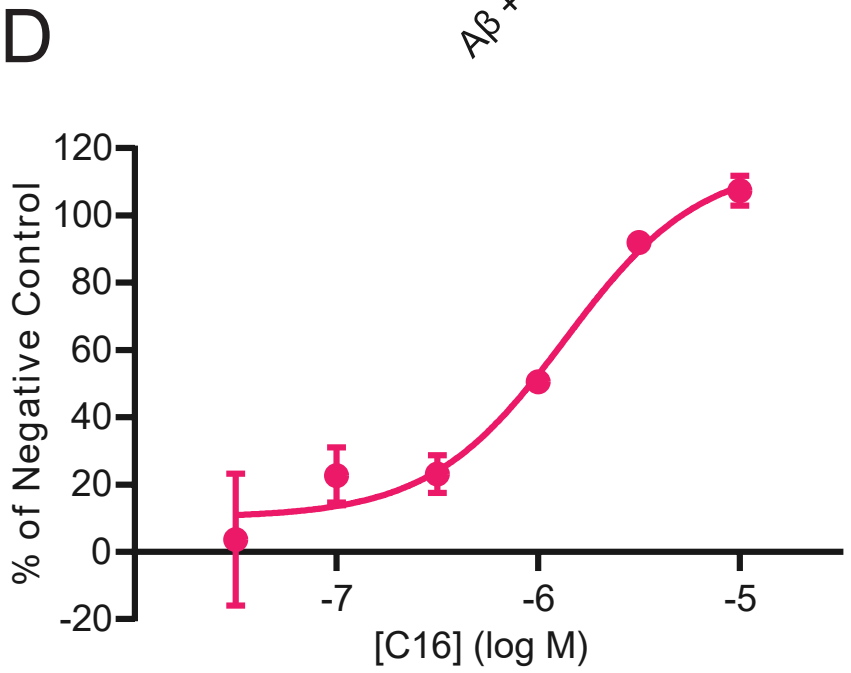
D
120
100
80
60
40
20
0
-20
% of Negative Control
-7
-6
-5
[C16] (log M)

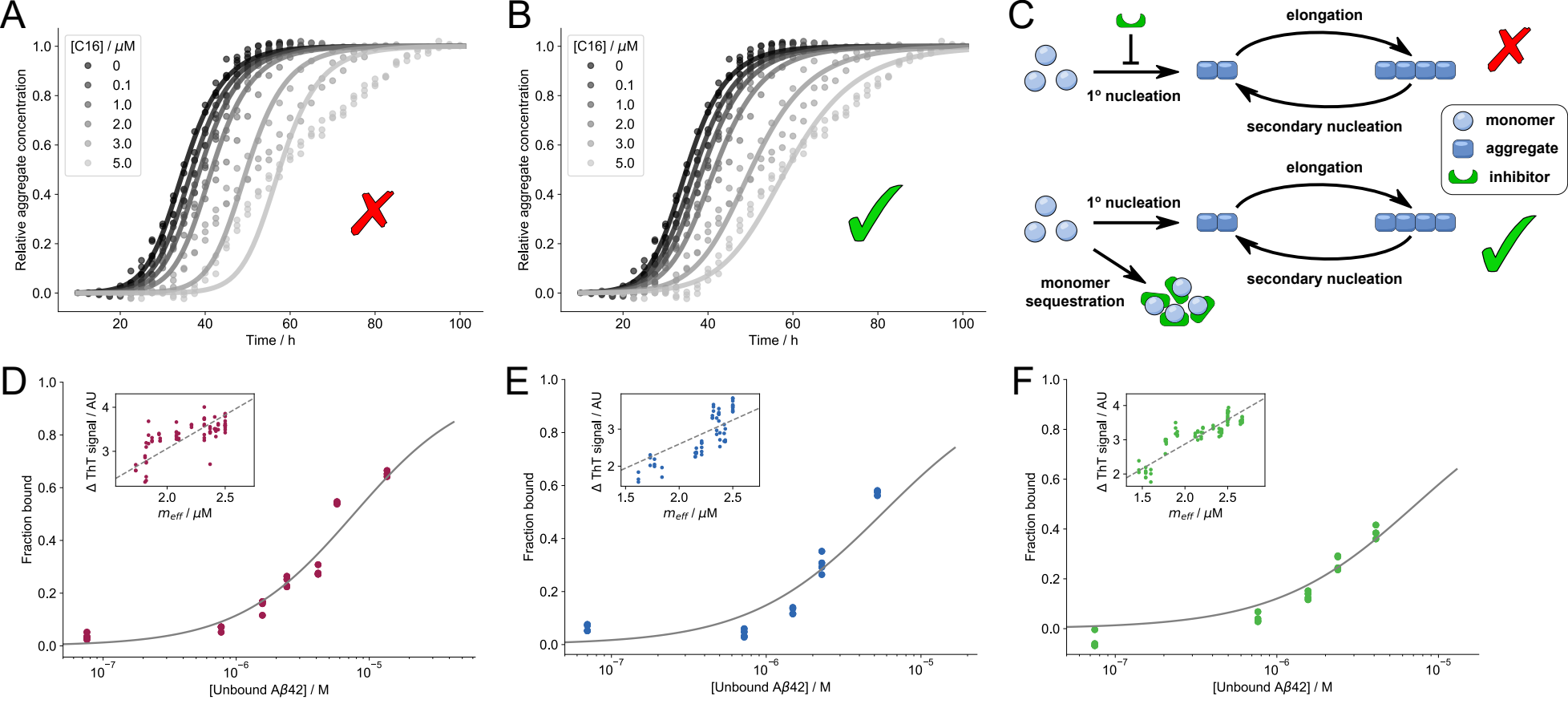
A
B
C
D
E
F
[C16] / μM
0
0.1
1.0
2.0
3.0
5.0
Relative aggregate concentration
Time / h
elongation
1° nucleation
secondary nucleation
monomer
aggregate
inhibitor
monomer sequestration
Fraction bound
Δ ThT signal / AU
m_{eff} / μM
[Unbound Aβ42] / M

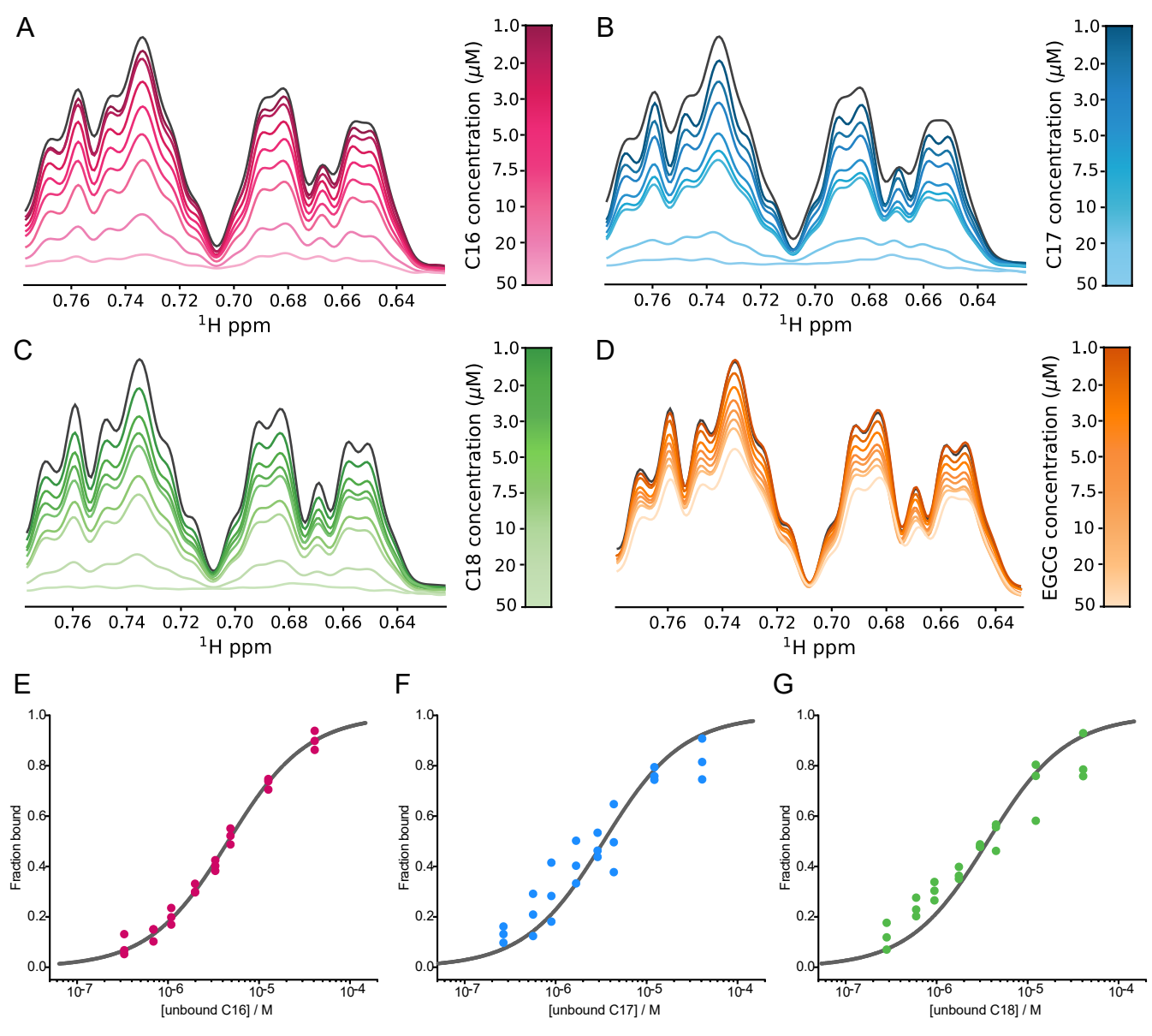
A
B
C
D
E
F
G
C16 concentration (μM)
C17 concentration (μM)
C18 concentration (μM)
EGCG concentration (μM)
1.0
2.0
3.0
5.0
7.5
10
20
50
0.76
0.74
0.72
0.70
0.68
0.66
0.64
1H ppm
Fraction bound
0.0
0.2
0.4
0.6
0.8
1.0
10-7
10-6
10-5
10-4
[unbound C16] / M
[unbound C17] / M
[unbound C18] / M